

The failure mechanism at adiabatic shear bands of titanium alloy: High-precision survey using precession electron diffraction and geometrically necessary dislocation density calculation

Xin Liu^{a,b}, Yu Zhou^{a,b}, Xinjie Zhu^{a,b}, Duoduo Wang^{a,b}, Qunbo Fan^{a,b,*}

^a School of Materials Science and Engineering, Beijing Institute of Technology, Beijing 100081, China

^b National Key Laboratory of Science and Technology on Materials under Shock and Impact, Beijing Institute of Technology, Beijing 100081, China



ARTICLE INFO

Keywords:

Adiabatic shear band (ASB)
Precession electron diffraction (PED)
Geometrically necessary dislocation (GND)
Density
Titanium alloy

ABSTRACT

The difficulty of obtaining key information, such as the crystal orientation and geometrically necessary dislocation (GND) density distribution, from a large deformation region in an adiabatic shear band (ASB) has hindered further study of the ASB failure mechanism in titanium alloys. In this work, the crystal orientation information of the failure position and surrounding region in ASB of a Ti-5Al-2.5Cr-0.5Fe-4.5Mo-1Sn-2Zr-3Zn alloy was obtained via transmission electron microscopy (TEM) and precession electron diffraction (PED) with a high spatial resolution. The GND density distribution was calculated and the adiabatic shear failure mechanism was revealed from the collected data. ASBs (original width: $\sim 3\text{--}4\ \mu\text{m}$) formed in the cylinder sample during dynamic compression (strain rate: $\sim 3000\ \text{s}^{-1}$). In the transition region at the edge of ASB, the grains were severely elongated along the direction parallel to the ASB boundaries with an average grain size on the order of μm and an average GND density of $5.5374 \times 10^{15}/\text{m}^2$ in the α phase. Relatively strong $< 0001 \rangle$ textures and weak $< -12\text{--}10 \rangle$ textures were observed. However, significant dynamic-recrystallization-dominated grain refinement in ASB, especially at the crack tip, resulted in many ultrafine equiaxed recrystallized grains (10 nm level) and weakened textures. The highest average GND density ($8.6242 \times 10^{15}/\text{m}^2$, in α phase) occurred in the crack tip region. Moreover, the vicinity of the "primary microcracks" in the main crack extension line was characterized by combinations of an extremely high GND density work hardening region and a group of low GND density recrystallized grains. This indicates that cracks in the ASB were initiated by the deformation incompatibility between the antecedent recrystallization region and the surrounding high work hardening region.

1. Introduction

Adiabatic shear bands (ASBs) are local regions characterized by severe plastic flow due to plastic instability caused by strain softening of materials [1–3]. Adiabatic shear localization often leads to the failure of many materials (e.g., steel [4,5], magnesium alloys [6], aluminum alloys [7], and titanium (Ti) alloys [8,9]) under high strain-rate loading. This is especially true for materials with low thermal conductivity, e.g., Ti and its alloys [6]. Therefore, the mechanism of localized adiabatic shear in Ti alloys has received significant attention. In recent years, the microstructural evolution in the ASB has been extensively studied with the aim of developing new high-performance Ti alloys suitable for high-strain-rate service environments [10,11]. These studies have focused on revealing the cause and main mechanism of adiabatic shearing in Ti alloys. Adiabatic shear failure is commonly attributed to thermal softening [10,12,13]. In recent years,

microstructure softening mechanisms, such as dynamic recrystallization (DRX), have in addition to thermal softening, been cited as major factors in adiabatic shear failure [11,14,15]. In some materials, e.g., Ti-6Al-4V and pure titanium, DRX (rather than thermal softening) is considered the dominant factor in this failure [16,17].

To observe the microstructure comprising ASBs in Ti alloys, hat-shaped or cylindrical samples were normally deformed at high strain rates using split Hopkinson bars. The microstructures were then usually observed via (for example) scanning electron microscopy (SEM) and transmission electron microscopy (TEM) [18–21]. Studies have revealed that the shape of ASBs in or the adiabatic shear sensitivity of Ti alloys varies with the microstructure of the material. Yang et al. [22] reported that, for the same strain rate, a $\alpha + \beta$ lamellar microstructure is more susceptible to adiabatic shear localization deformation than the β phase microstructure. Similarly, Liu et al. [23] have shown that a bimodal microstructure is more susceptible to adiabatic shear

* Corresponding author at: School of Materials Science and Engineering, Beijing Institute of Technology, Beijing 100081, China.

E-mail address: fanqunbo@bit.edu.cn (Q. Fan).

<https://doi.org/10.1016/j.msea.2019.01.016>

Received 4 December 2018; Received in revised form 3 January 2019; Accepted 4 January 2019

Available online 05 January 2019

0921-5093/© 2019 Elsevier B.V. All rights reserved.

localization deformation than a lamellar microstructure. The grains in a shear band are generally smaller than the grains in the surrounding matrix, and may be accompanied by microcrack initiation in the local region. Severe plastic deformation during shear band formation may lead to grain refinement and subsequent recrystallization [1,24], which results in microcrack initiation in the softening region [6,10]. Yang et al. [25] and Kuang et al. [26] investigated the adiabatic shear processes in a near-beta Ti alloy Ti-1300 and pure Ti, respectively. The results revealed that rotational dynamic recrystallization (RDRX) in these materials leads to the formation of ultrafine grains within the shear band. Zhan et al. [27] characterized, via TEM, the microstructure within ASB of metastable β -Ti alloy Ti6554 exposed to high strain rates and elevated temperatures. They found that a low volume fraction of DRX nanograins occurs in the core region of ASB and suggested that the dislocation activity plays a dominant role in the grain refinement process within the ASB of this alloy. Li et al. [28] investigated ultrafine-grained (~ 120 nm) pure Ti via TEM and found that the central regions of ASB gave rise to diffraction rings, consistent with the presence of ultrafine grains (~ 40 nm) within ASB. However, the acquisition of further information (e.g., the specific orientation and dislocation density of each grain) was prevented, owing to limitations of the equipment. The microstructural evolution and mechanism of adiabatic shear failure are understood to a certain degree. Nevertheless, full revelation of the underlying mechanism governing this failure remains elusive, as the information available (e.g., on the crystal orientations and dislocation densities) is insufficient.

The crystallographic orientation of the grains has a significant effect on the deformation behavior of a material [29]. Understanding the evolution of crystal orientations in the ASB is crucial for a complete understanding of the adiabatic shear failure mechanism [30–32]. As the most effective method of determining the single crystal orientation of crystal materials, electron backscatter diffraction (EBSD) has also been used to investigate the crystal orientations in shear bands [33]. Wang et al. [30] studied the high strain rate deformation of a coarse-grained beta Ti alloy, Ti-5Al-5Mo-5V-1Cr-1Fe. The results revealed that the core of the ASB, which consists of ultrafine (width: $0.1 \mu\text{m}$) deformed grains and a high density of dislocations, is characterized by a fiber texture. Jiang et al. [31] found that the microstructure of pure Ti within ASB consists of ultrafine grains ($0.1\text{--}1 \mu\text{m}$) with well-defined high-angle-boundaries, and the $\langle 11\text{--}20 \rangle$ direction is (in general) aligned with the local shear direction. Yang et al. [32] calculated (from EBSD data) the strain field within the ASB and the neighboring region. The results revealed that the largest strain occurs in the ASB region, i.e., the preferred site for nucleation. However, the EBSD techniques have limited spatial resolution. For example, the spatial resolution of EBSD in slightly deformed materials and highly deformed materials is $20\text{--}30$ nm [34] and 100 nm [35], respectively. The results of the EBSD test would also be affected by residual deformation, i.e., low-quality EBSD patterns are obtained, owing to the large (severe) deformation of the crystal lattice [30]. Therefore, EBSD investigation of tiny grains or severely deformed regions (e.g., nanocrystalline and crack tip positions [6,11]), which are characteristic of ASB, is difficult. Obtaining crystal orientation information via EBSD of these regions and calculating the GND density in corresponding regions are arduous. Hence, conventional research results of DRX-induced adiabatic shear failure are mostly based on indirect evidence such as numerical simulation [17,36]. In fact, the key microstructural characteristics of the failure position and surrounding region in ASB remain unclear.

In the precession electron diffraction (PED) technique [37], the beam is taken off-axis by the upper deflection coils and precessed about the optic axis for scanning at a constant precession angle. This is performed in combination with an opposite descan of the beam using the lower deflection coils located below the specimen, resulting in a diffraction pattern that is focused. The parallelism between the incident beam and zone axis where the strongest dynamical interactions occur is avoided and, hence, the effects of dynamic diffraction (e.g., multiple

diffraction and systematic intensity variations) are effectively eliminated. Thus, the spatial resolution can be improved ($3\text{--}5$ nm generally, 0.5 nm the minimum) compared with that of conventional EBSD and the crystal orientation information in a large deformation region can be more accurately obtained. Using high-resolution PED, Balachandran et al. [38] investigated recrystallization during hot compression of a Ti5553 alloy in the two-phase $\alpha + \beta$ regime and clearly distinguished between the globularization and conventional dynamic recrystallization of α . Mohseni et al. [39] characterized the orientation and texture of highly strained wear-induced ultrafine grains via PED. They analyzed the surface and subsurface structural evolution during sliding wear of two in situ nitrided Ti alloys, and found that the nitrided Ti-6Al-4V exhibited slightly increasing wear, despite higher hardness, due to shear band formation. Investigation of such problems via EBSD is difficult, but the use of PED technology for the study of ASB failure mechanisms is expected to yield new results.

In this work, the crystal orientation characteristics at the failure position and surrounding region in ASB of a high-strength high-toughness dual-phase Ti alloy, Ti-5Al-2.5Cr-0.5Fe-4.5Mo-1Sn-2Zr-3Zn (developed at Beijing University of Technology), are obtained via PED with a high spatial resolution. Based on these characteristics, the GND density distribution in the corresponding region is calculated. New direct evidence for revealing the underlying adiabatic shear failure mechanism is presented, providing a new means of investigating ASBs in Ti alloys.

2. Experimental procedures

In this study, a $\phi 80$ mm \times 290 mm forged Ti-5Al-2.5Cr-0.5Fe-4.5Mo-1Sn-2Zr-3Zn bar was obtained after six passes of forging at 860°C . An average pass deformation of 45% and double annealing ($880^\circ\text{C}/0.5$ h/FC + $740^\circ\text{C}/2$ h/FC) were employed during the process. The microstructures shown in Fig. 1 reveal the equiaxed structure (average grain size: $\sim 3 \mu\text{m}$) of the alloy. The basic mechanical properties of the alloy are as follows: yield strength: 986 MPa, tensile strength: 1048 MPa, and elongation: 17.7%.

Through wire-electrode cutting, cylinder samples ($\phi 4 \times 4$ mm) are cut from the annealed bars for a dynamic compression test (strain rate: ~ 3000 s $^{-1}$) using a split Hopkinson pressure bar (SHPB) at room temperature. Similar to the test method described in the literature [40], a stop ring (3.4 mm height) is used to control the strain and obtain an ASB-containing sample where failure is imminent.

A cross-sectional sample containing the ASB was prepared (via wire-electrode cutting) from a sample with an accumulated strain of 0.85 along the loading direction. The sample was mechanically ground,

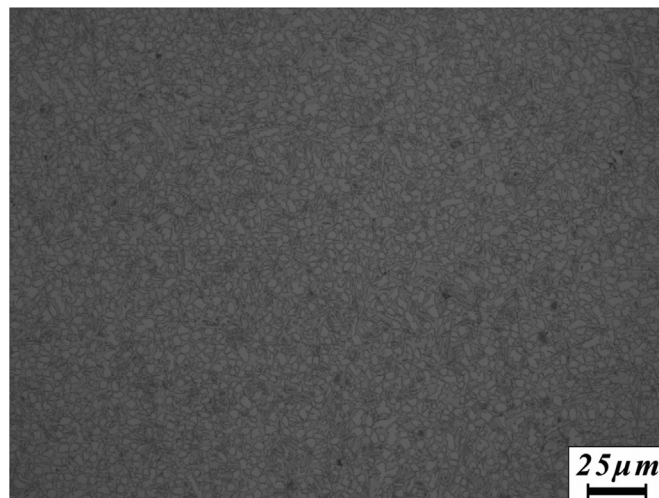


Fig. 1. Microstructure of forged Ti-5Al-2.5Cr-0.5Fe-4.5Mo-1Sn-2Zr-3Zn alloy.

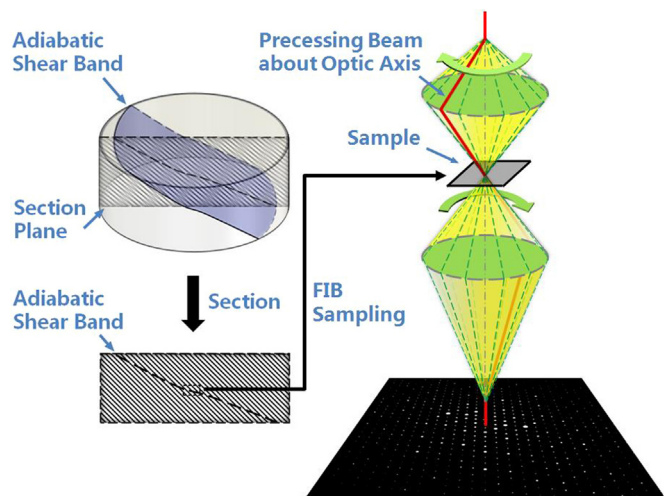
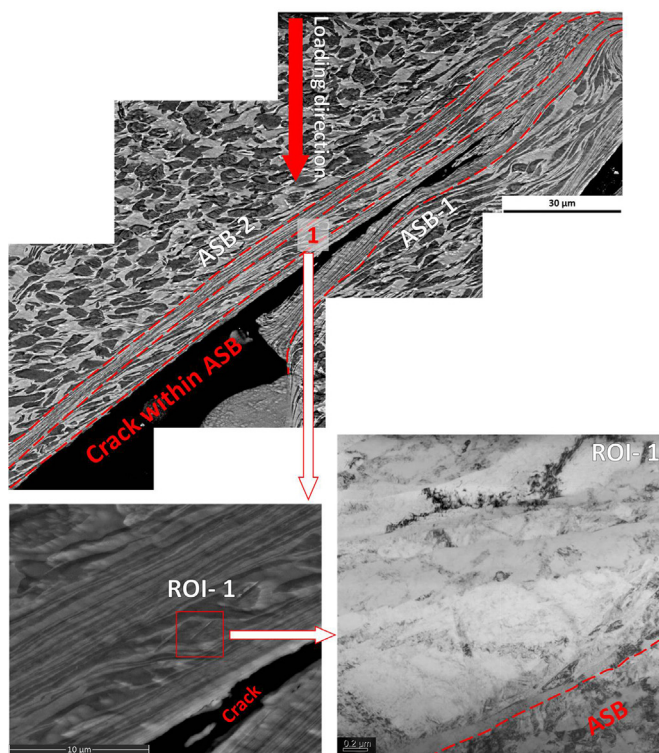


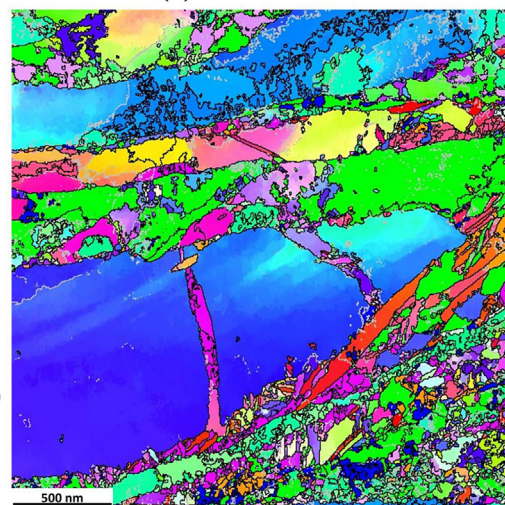
Fig. 2. Diagram of the microstructure characterization process.

Table 1
The dislocations types in α -Ti and the corresponding weight factors [48].

Slip system	Burgers vector	Edge		Screw	
		Number	Weight	Number	Weight
$\langle a \rangle$ -basal	$\langle 11\text{-}20 \rangle$	3	0.124	3	0.087
$\langle a \rangle$ -prismatic	$\langle 11\text{-}20 \rangle$	3	0.124	0	
$\langle a \rangle$ -pyramidal	$\langle 11\text{-}20 \rangle$	6	0.124	0	
$\langle c+a \rangle$ -pyramidal	$\langle 11\text{-}23 \rangle$	12	0.437	6	0.306



(a)



(b)

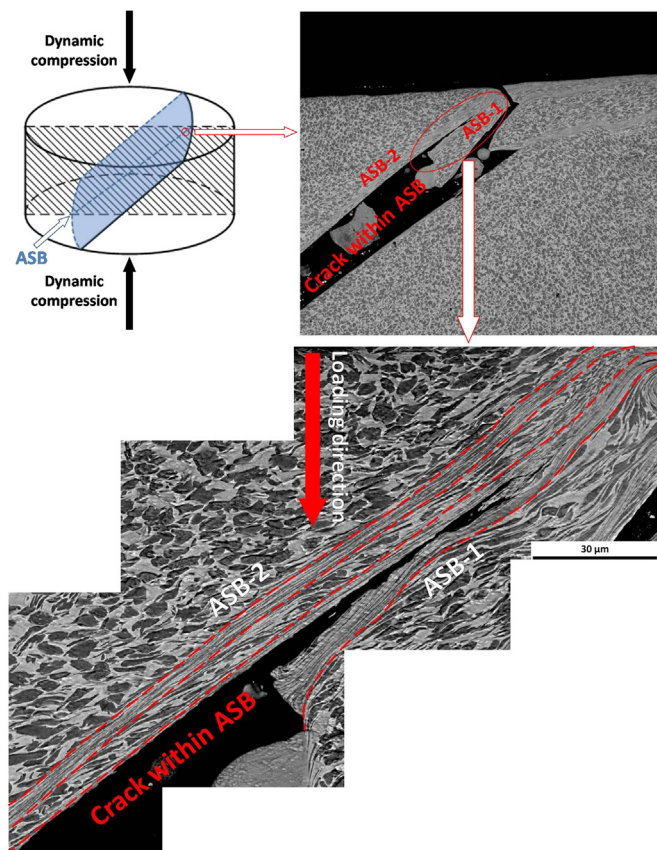


Fig. 3. Location and morphology of the ASB region.

Fig. 4. The (a) location, bright-field TEM imaging, and (b) OIM of ROI-1.

electro-polished, and then further etched (in a diluted solution of 2 HF:10 HNO₃:88H₂O) for the preliminary SEM observation (FEI Nova Nanosem 430 field emission scanning electron microscope) at 20 kV.

A focused ion beam (FIB) was used to prepare the cross-sectional TEM samples from the regions of interest (ROIs) on the section plane. To effectively avoid the ion-beam induced damage, the specimen preparation was carefully performed in an FEI Helios Nanolab 600i DualBeam (FEI Company, Hillsboro, Oregon, USA). Both electron beam and ion beam was used to deposit the protective layer to balance the damage and efficiency. This is because electron-beam-deposition has no damage on the sample and its efficiency is low, while the efficiency of ion-beam-deposition is high. Initially, a 0.5 μm layer of platinum coating was deposited on the ROI via electron beam in order to protect it from sputtering of the ion beam during lamella fabrication, and then 1 μm platinum layer was deposited via ion beam on the deposited

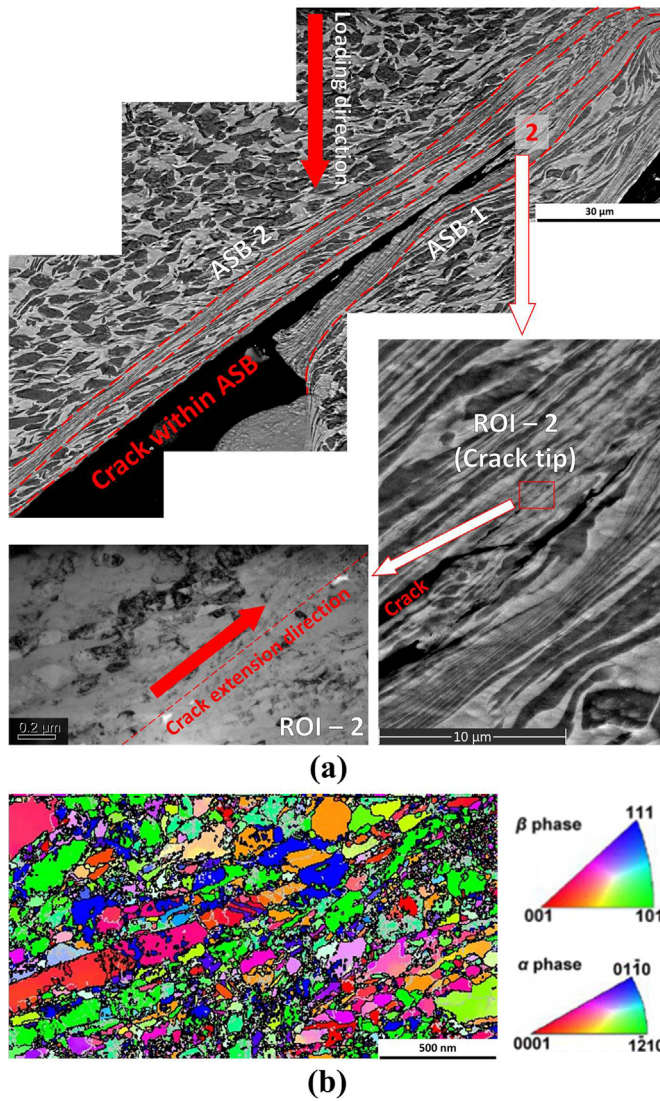


Fig. 5. The (a) location, bright-field TEM imaging, and (b) OIM of ROI-2.

0.5 μm platinum layer. The V-groove cut with two rectangle patterns separated the lamella from the bulk, the micromanipulator was attached to the lamella and each end of the lamella was cut off. Subsequently, the lamella was transferred to a TEM grid and cut free from the micromanipulator. Hereafter, it was milled to a thickness of approximately 50 nm using the FIB. It might be mentioned that the beam energy was decreased from 30 kV to lower voltages during the milling process, with a final voltage as low as 2 kV which has an ultrathin damage layer with only 2 nm in thickness, so as to clean up the specimen. More details can be found in various other articles [41,42].

Subsequently, orientation imaging microscopy was performed on the FIB samples using an FEI Tecnai G2 F20 S-Twin FEG scanning/transmission electron microscope (FEI, Hillsboro, MO, USA) with a PED control unit (DigiSTAR P1000 system, NanoMEGAS Sprl, Brussels, Belgium) operating at 200 kV. A diagram of the entire process is shown in Fig. 2. A converged beam (diameter: ~ 1 nm) was precessed about the optic axis at an angle of 0.65° (PED step size: 4.2 nm). Afterward, the collected data was exported into a commercial software HKL CHANNEL5 (Oxford Instruments, Halifax Road, High Wycombe, BUCKS, HP12 3SE, UK) for analysis.

In this paper, we used a program that is implemented in MatLab software to extract and calculate GNDs from PED data. The theory of the Nye tensor α_{ij} described in the work of Nye, Arsenlis, and Pantleon

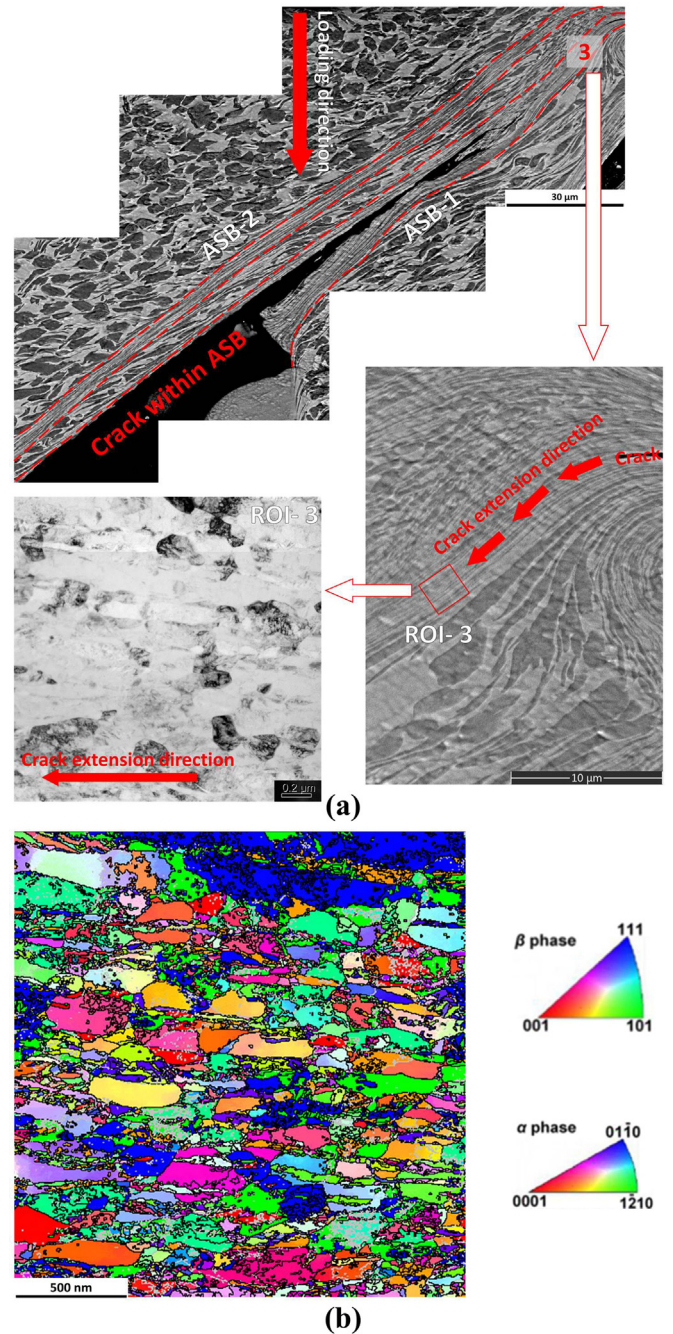


Fig. 6. The (a) location, bright-field TEM imaging, and (b) OIM of ROI-3.

et al. [43–45] is used to calculate the GND density ρ_{GND} . Referring to the detailed calculation steps in previous work [46], we consider all the 33 types of potential dislocations in α -Ti (Table 1), and a minimization energy criterion is used to identify unknown GNDs that accommodate a given lattice curvature [47]:

$$L^1 = \sum_{k=1}^N |\rho_{GND}^k w^k| \quad (1)$$

Where, N is the number of all possible types of dislocation and w^k is the weight factor corresponding to the dislocation type.

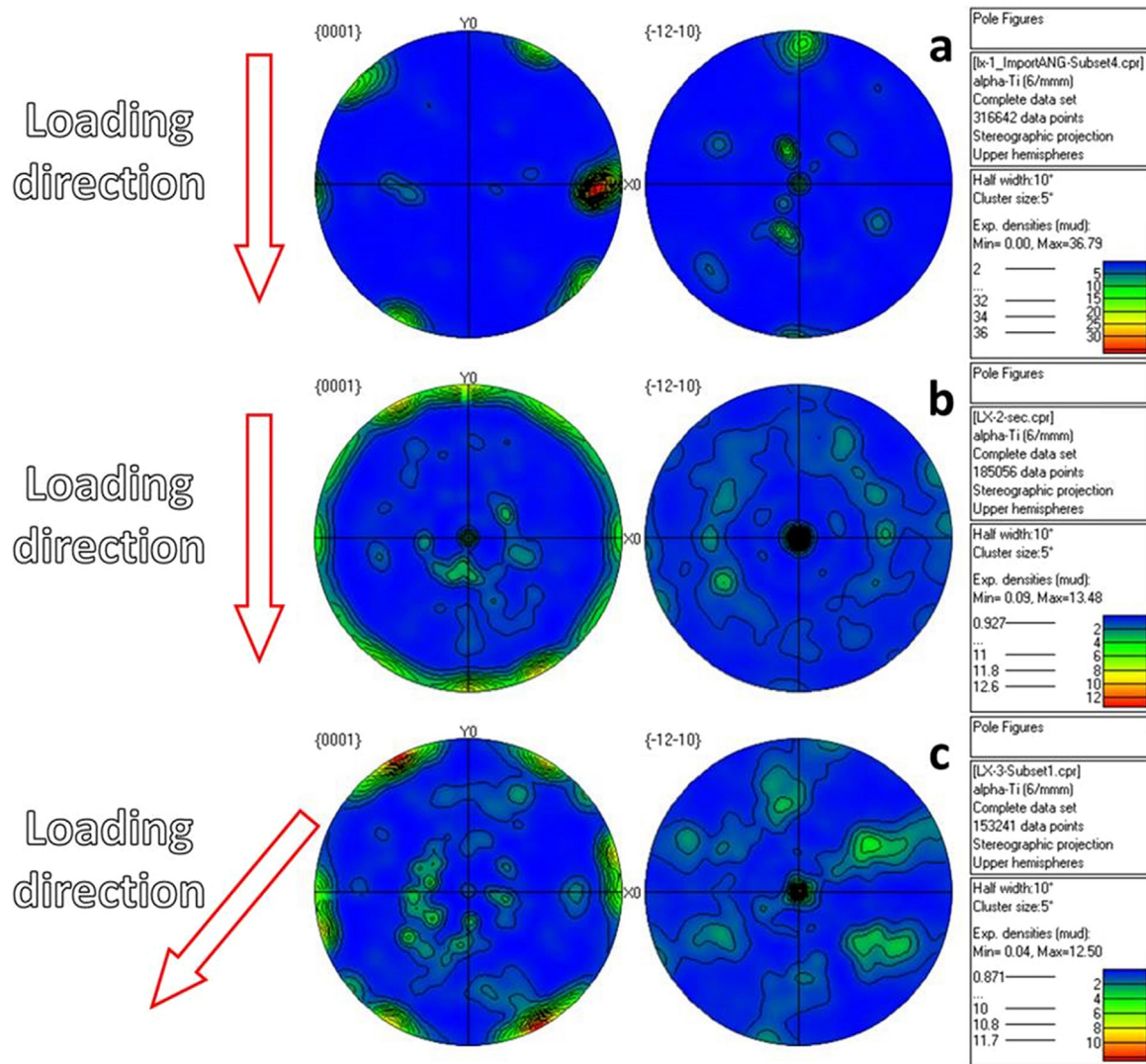


Fig. 7. Pole figures corresponding to (a) ROI-1, (b) ROI-2, (c) ROI-3.

3. Results and discussion

3.1. Microstructure

During dynamic compression, ASBs eventually form at an angle of 45–55° to the loading direction and microcracks nucleate, grow, and coalesce in these ASBs, leading to failure of the sample (see Fig. 3). This microstructural evolution results in spatially heterogeneous microstructural characteristics of the sample. Two ASBs occur at the edge of the specimen where crack coalescence is incomplete. One of these (denoted as ASB-1 in Fig. 3) contains part of the main crack of the specimen, where critical failure is imminent, whereas the other (denoted as ASB-2 in Fig. 3) is crack free. ASB-1 is selected for subsequent investigation and, hence, the subsequently mentioned terms "shear band" or "ASB" refer to ASB-1. As Fig. 3 shows, ASB with an original width of ~3–4 μm is widened, owing to the coalesced crack. In Figs. 4–6, the main region-of-interests (ROIs) are indicated by red numbers. ROI-1 corresponds to the transition region between ASB and the surrounding area, and ROI-2 corresponds to the crack tip (i.e., the key position of adiabatic shear failure) in the ASB region. Similarly, ROI-3 corresponds to the typical crack-free region that is located on the extension line of the main crack.

Fig. 4 shows the location, bright-field TEM imaging (Fig. 4a), and orientation image (OIM, Fig. 4b) of ROI-1. In each OIM, high-angle

grain boundaries ($\geq 15^\circ$, HAGBs) and phase boundaries are depicted as black lines and low-angle grain boundaries ($< 15^\circ$, LAGBs) are depicted as grey lines. The grains in the transition region are severely elongated along the direction parallel to the ASB boundaries and are considerably larger (reaching the μm level) than those in ASB. This results mainly from the large strain and high temperature in the ASB. Moreover, the number of heterogeneously distributed subgrain boundaries occurring in the large grains in the transition region is slightly larger than that occurring in ASB.

Fig. 5 shows the location, bright-field TEM imaging (Fig. 5a), and OIM (Fig. 5b) of ROI-2. This region contains many recrystallized grains and subgrains with an average size of 10–100 nm and most of these grains are equiaxed. For example, the region along the "crack extension direction" (denoted by the red dashed line in the magnified image of the "crack tip" region in the lower left of Fig. 5a) consists mainly of 10 nm (diameter) equiaxed nanograins. On both sides, the deformation is more pronounced in the larger grains than in the smaller grains, and the subgrain boundaries are more widely distributed than those in ROI-1. These LAGBs formed during the deformation and recovery process, and will transform into HAGBs during further deformation. Intensive recrystallization occurs in the ASB area to be fractured (i.e., crack coalescence is imminent), with relatively significant deformation in the surrounding region.

Fig. 6 shows the location, bright-field TEM imaging (Fig. 6a), and

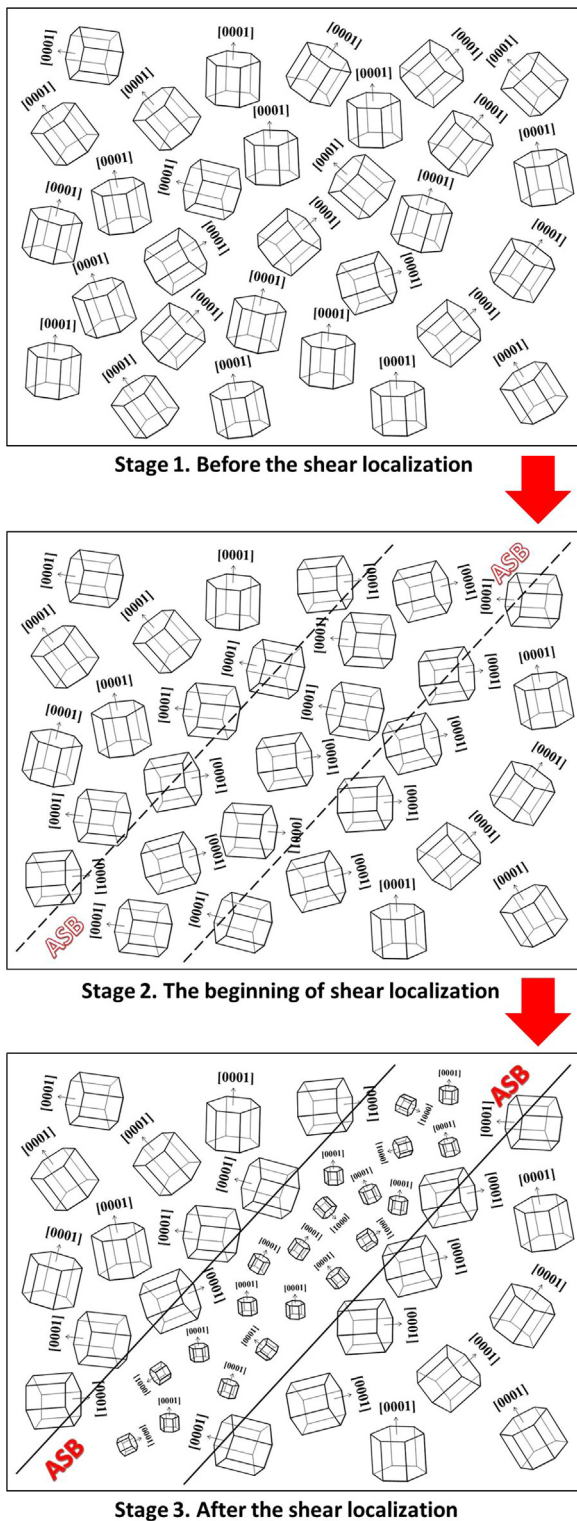


Fig. 8. Schematic showing the evolution of the crystal orientations.

OIM (Fig. 6b) of ROI-3. This region, similar to ROI-2, consists of many recrystallized (sub)grains, with an average size of 10–100 nm. However, the overall grain size of ROI-3 is larger than that of ROI-2, tensile deformations of grains along the shear direction are more pronounced, and volume fraction of recrystallized grains is smaller; in addition, the number of subgrain boundaries is lower, consistent with smaller deformation and less intensive induced recrystallization in the crack-free region of ASB. In many grains, the recrystallized (sub)grains form a

necklace structure, which is usually considered one of the characteristics of DRX. This suggests that DRX dominates the grain refinement process of ASB in this alloy.

An ASB is subjected to larger strain at a higher strain rate than the surrounding region, resulting in a significant adiabatic temperature rise. This temperature rise will lead to grain coarsening and promote recrystallization, thereby resulting in grain refinement. Severe deformation will also lead to grain refinement. Previous results suggest that the competition between grain coarsening and grain refinement yields a decrease in the average grain size in ASB. In general, the grains in ASB are mainly equiaxed nano-grains resulting from large deformation and DRX. The numbers of recrystallized equiaxed grains decrease (in general) with increasing distance from ASB, i.e., fewer of these grains occur in the transition region than in ASB.

3.2. Texture and orientation misorientation distribution

Fig. 7 shows the $\{0001\}$ and $\{-12\cdot10\}$ pole figures corresponding to each ROI. A high concentration of $\{0001\}$ poles occurs in the direction perpendicular to the compression direction near ASB (ROI-1, Fig. 7a). However, this texture is weakened within ASB (e.g., ROI-3, Fig. 7c) due to the many dynamically recrystallized grains, especially at the crack tip (ROI-2, Fig. 7b). Moreover, some $\langle -12\cdot10 \rangle$ directions rotated away from the compression direction during deformation, leading to a decrease in the concentration of $\{-12\cdot10\}$ poles, except in the normal direction of the longitudinal section.

A comparison of the textures characterizing each ROI (see Fig. 8 for schematic showing the evolution of the crystal orientation) reveals no preferred crystal orientation in the sample prior to shear localization (stage 1). Moreover, during the early stage of shear localization (stage 2), the $\langle 0001 \rangle$ directions are, in general, perpendicular to the compression direction in ASB and the surrounding region. Subsequently, when the temperature and amount of deformation are increased, several grain orientations arise in ASB, owing to the formation of many new grains with orientations differing from those of their respective parents (stage 3). The number of grain orientations increases with increasing intensity of the recrystallization (e.g., in the region near the initiation point of microcracks).

The misorientation distributions of the ROIs are shown as histograms in Fig. 9. The fraction of LAGBs and the fraction of HAGBs, respectively, are summarized as follows: ROI-1 α phase (Fig. 9a): 26.76% and 73.24%, β phase (Fig. 9b): 41.31% and 58.69%; ROI-2 α phase (Fig. 9c): 30.57% and 69.43%, β phase (Fig. 9d): 73.63% and 26.37%; ROI-3 α phase (Fig. 9e): 24.57% and 75.43%, β phase (Fig. 9f): 22% and 78%. In most regions of ASB, the fraction of HAGBs is higher than the fraction of LAGBs, substantiating the occurrence of DRX during adiabatic shear. However, in the crack tip (ROI-2), the fraction of HAGBs is lower than the fraction of LAGBs. This may have resulted from the more intense deformation in the crack tip and the surrounding region, compared with the deformation in other regions.

3.3. GND density distributions

Figs. 10–12 show the morphology and corresponding GND density distribution of the α phase in ROI-1, ROI-2, and ROI-3, respectively. For the convenience of contrast, the left image shows the TEM morphology of each ROI (Fig. 10a–Fig. 12a) and the right image (Fig. 10b–Fig. 12b) is obtained by overlapping (based on their spatial location-relation) the corresponding GND density distribution of the α phase with the TEM morphology. The relevant GND density statistics are obtained via the calculation method described in Section 2. The average GND density of the α phase is summarized as follows: ROI-1: $5.5374 \times 10^{15}/\text{m}^2$, $3.1569 \times 10^{15}/\text{m}^2$ for $\langle a \rangle$ dislocations and $2.3805 \times 10^{15}/\text{m}^2$ for $\langle a+c \rangle$ dislocations; ROI-2: $8.6242 \times 10^{15}/\text{m}^2$, $5.0842 \times 10^{15}/\text{m}^2$ for $\langle a \rangle$ dislocations and $3.54 \times 10^{15}/\text{m}^2$ for $\langle a+c \rangle$ dislocations; ROI-3: $7.4746 \times 10^{15}/\text{m}^2$, $4.7702 \times 10^{15}/\text{m}^2$ for $\langle a \rangle$

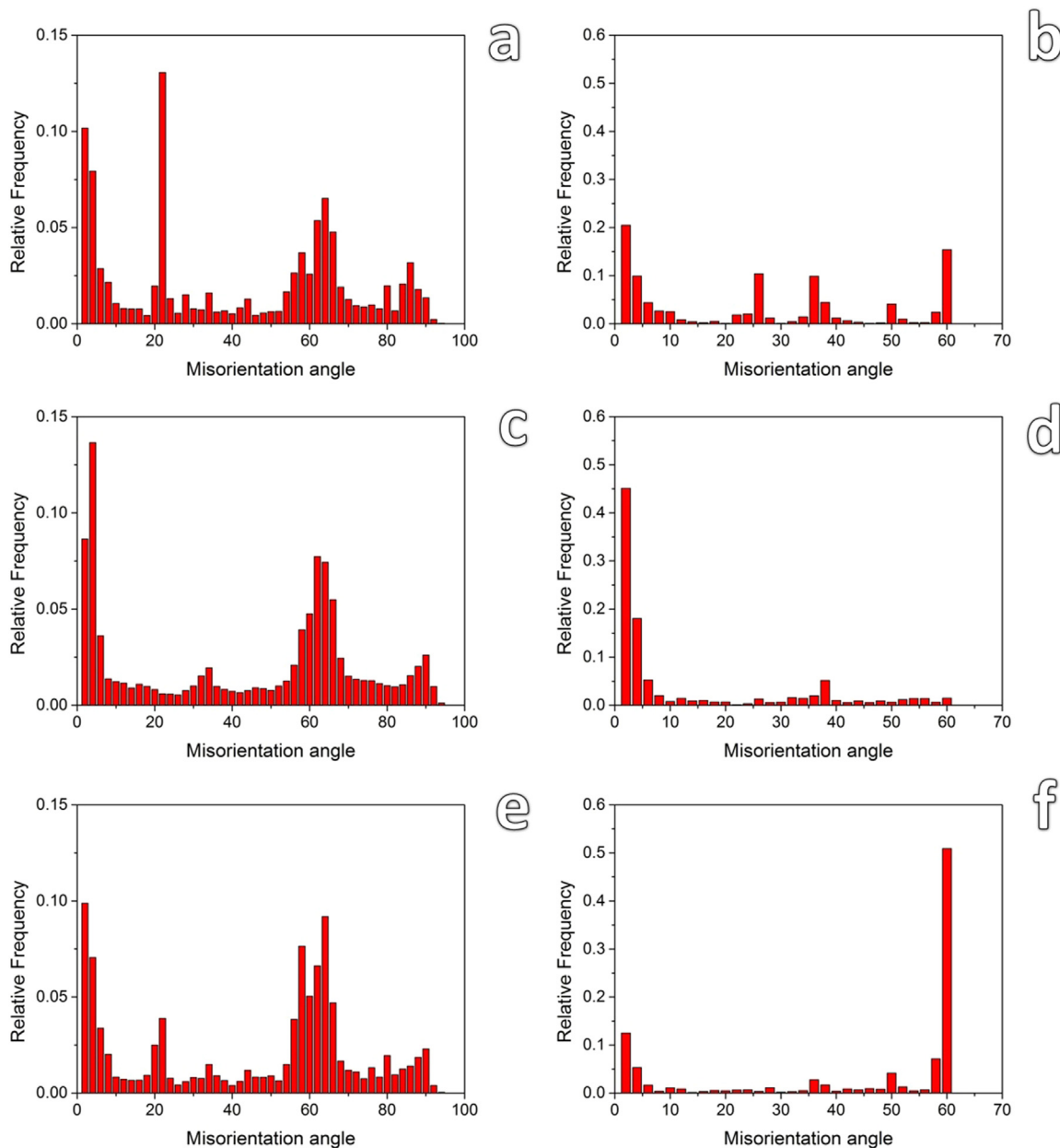


Fig. 9. Misorientation distributions of ROIs: (a), (c), (e) α phase and (b), (d), (f) β phase in ROI-1, ROI-2, and ROI-3, respectively.

dislocations and $2.7044 \times 10^{15}/\text{m}^2$ for $\langle a+c \rangle$ dislocations.

As the above statistics show, the GND density of the α phase in ROI-1 is quite low, as indicated by the large blue and green region in Fig. 10(b). Combining with Fig. 4(b) reveals that the GND density is relatively high at grain boundaries and subgrain boundaries, but relatively low inside the grains. Moreover, the GND densities on LAGBs are usually higher than in other regions. The GND density of the α phase in ROI-2 is considerably higher than that of the α phase in ROI-1, as indicated by red and yellowish green areas scattered along the crack extension direction. In ROI-3, the GND density of the α phase is slightly lower than that of ROI-2 and significantly higher than that of ROI-1. Similarly, the LAGBs are denser than those in ROI-1, which is consistent with the statistical results shown in Fig. 9. A higher fraction of LAGBs occur in the α phase than in the OIM (Fig. 6(b)). In all ROIs, the density of $\langle a \rangle$ type dislocations is significantly higher than that of $\langle a+c \rangle$ type dislocations. This indicates that the $\langle a \rangle$ type slip systems operate more easily than $\langle a+c \rangle$ type slip systems, which is consistent with the results reported in other studies [49].

In general, the distribution of dislocation cells is non-uniform and the GND density of the α phase in ASB is relatively high, especially in the area to be fractured. In fact, the corresponding TEM morphology near several red (i.e., high GND density) regions in ROI-2 (Fig. 11(b)) reveal the regular arrangement of discontinuous tiny white "voids" along the crack extension line. These voids are, in fact, microcracks in the early stage of initiation (Fig. 11a).

Compared with that of ROI-2 (Fig. 5), the GND density associated with the group of ultrafine equiaxed recrystallized grains is low, whereas the adjacent high GND density region consists of many substructures (e.g., subgrains). The positions of this combination of low GND density recrystallized grains (indicative of relative microstructure softening) and adjacent high GND density regions (consistent with severe work hardening) is basically consistent with that of the aforementioned primary microcracks in the main crack extension line.

Considering the aforementioned orientation, morphology, and GND density distribution, a new direct evidence for revealing the underlying adiabatic shear failure mechanism is presented. As shown in Fig. 13,

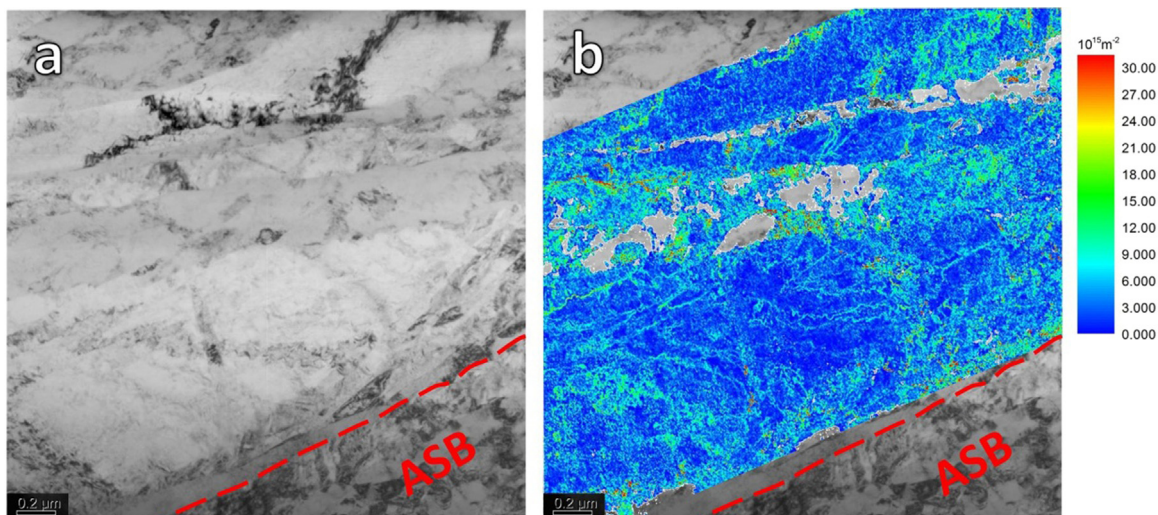


Fig. 10. Contrast between the (a) TEM morphology and (b) corresponding GND density distribution of the α phase in ROI-1.

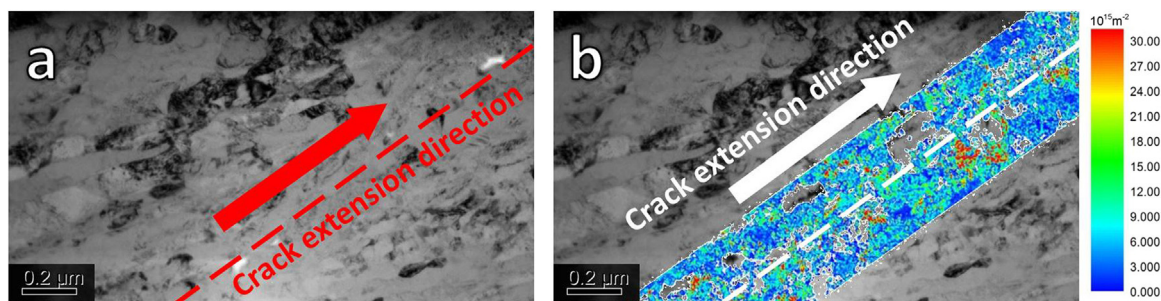


Fig. 11. Contrast between the (a) TEM morphology and (b) corresponding GND density distribution of the α phase in ROI-2.

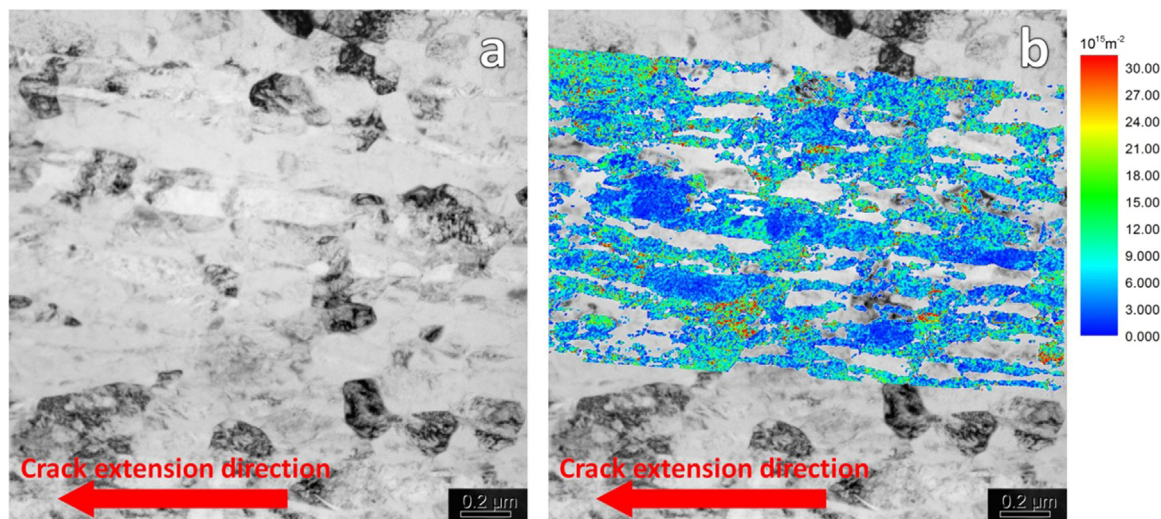


Fig. 12. Contrast between the (a) TEM morphology and (b) corresponding GND density distribution of the α phase in ROI-3.

microcrack initiation in ASB, owing to the incompatibility between the group of ultrafine equiaxed recrystallized grains and the adjacent high work hardening region is assumed. Microcracks occur in different regions of ASB, and then propagate and coalesce, resulting in the failure of the material. This is consistent with the study of pure Ti by Landau et al. [16]. Similarly, this evidence strongly supports the claims of Rodríguez-Martínez et al. [50] and Rittel et al. [11] that microstructure softening precedes adiabatic shear failure and is the dominant micro-mechanical factor in adiabatic shear. In addition, thermal softening

may also play a key role in promoting adiabatic shear in materials with very late DRX onset [14].

4. Conclusion

In this work, the crystal orientation information of the failure position and surrounding region in ASB of a high-strength high-toughness dual-phase Ti alloy, Ti-5Al-2.5Cr-0.5Fe-4.5Mo-1Sn-2Zr-3Zn, is obtained via PED with a high spatial resolution. The GND density distribution of

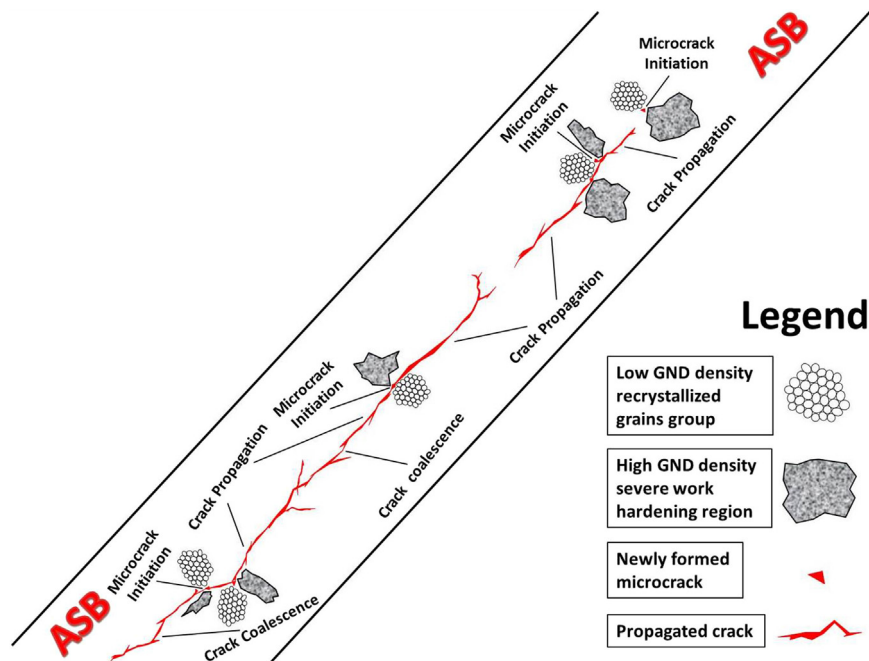


Fig. 13. Schematic of the crack evolution in ASB.

the respective regions is calculated and the adiabatic shear failure mechanism is identified from the collected data. The results reveal that significant DRX-dominated grain refinement occurs in ASB. For example, an average grain size on the order of μm occurs in the transition region, whereas average sizes of 10–100 nm occur inside the ASB. Groups of ultrafine equiaxed recrystallized grains (10 nm level) occur in the crack tip region. In addition, the transition zone is characterized by textures due to shear localization and the ASB region is described by DRX-weakened versions of these textures. The statistics also show that the average GND density ($7.4746 \times 10^{15}/\text{m}^2$) of ASB is significantly higher than that ($5.5374 \times 10^{15}/\text{m}^2$) of the transition zone, with the highest average density ($8.6242 \times 10^{15}/\text{m}^2$) occurring in the crack tip region. In the vicinity of each microcrack, a high GND density region is often accompanied by a group of recrystallized grains with low GND density. This indicates that the adiabatic shear failure of the alloy is initiated by the deformation incompatibility between the antecedent recrystallization region (low GND density) and the surrounding high work hardening region (extremely high GND density).

Acknowledgments

This work was financially supported by the National Natural Science Foundation of China (Grant No. 51571031). Dr. Zheng from ZKKF (Beijing) Science & Technology Co., Ltd is acknowledged for EBSD tests and data analysis.

Data availability

The raw/processed data required to reproduce these findings cannot be shared at this time due to technical or time limitations.

References

- [1] M.A. Meyers, G. Subhash, B.K. Kad, et al., Evolution of microstructure and shear-band formation in α -hcp titanium, *Mech. Mater.* 17 (2–3) (1994) 175–193.
- [2] M.A. Meyers, H.R. Pak, Observation of an adiabatic shear band in titanium by high-voltage transmission electron microscopy, *Acta Metall.* 34 (12) (1986) 2493–2499.
- [3] B. Dodd, Y. Bai, *Adiabatic Shear Localization*, (2012).
- [4] A.A. Tiarniyu, M. Eskandari, M. Sanayei, et al., Mechanical behavior and high-resolution EBSD investigation of the microstructural evolution in AISI 321 stainless steel under dynamic loading condition, *Mater. Sci. Eng. A* 673 (2016) 400–416.
- [5] S. Boakye-Yiadom, A.K. Khan, N. Bassim, A systematic study of grain refinement during impact of 4340 steel, *Mater. Sci. Eng. A* 605 (6) (2014) 270–285.
- [6] D. Rittel, Z.G. Wang, Thermo-mechanical aspects of adiabatic shear failure of AM50 and Ti6Al4V alloys, *Mech. Mater.* 40 (8) (2008) 629–635.
- [7] T. Kozmel, M. Vural, S. Tin, EBSD characterization of shear band formation in aluminum armor alloys, *J. Mater. Sci.* 51 (16) (2016) 7554–7570.
- [8] W.S. Lee, C.F. Lin, T.H. Chen, et al., Correlation of dynamic impact properties with adiabatic shear banding behaviour in Ti–15Mo–5Zr–3Al alloy, *Materials Science & Engineering A*, 475 (1) (2008) 172–184.
- [9] S.V. Kailas, Y.V.R.K. Prasad, S.K. Biswas, Flow instabilities and fracture in Ti-6Al-4V deformed in compression at 298 K to 673 K, *Metall. Mater. Trans. A* 25 (10) (1994) 2173–2179.
- [10] C. Zener, J.H. Hollomon, Effect of strain rate upon plastic flow of steel, *J. Appl. Phys.* 15 (1) (1944) 22–32.
- [11] D. Rittel, P. Landau, A. Venkert, Dynamic recrystallization as a potential cause for adiabatic shear failure, *Phys. Rev. Lett.* 101 (16) (2008) 165501.
- [12] J. Li, Y. Li, C. Huang, On adiabatic shear localization in nanostructured face-centered cubic alloys with different stacking fault energies, *Acta Mater.* (2017) 141.
- [13] M.H. Miguélez, X. Soldani, A. Molinari, Analysis of adiabatic shear banding in orthogonal cutting of Ti alloy, *Int. J. Mech. Sci.* 75 (10) (2013) 212–222.
- [14] P. Longère, Respective/combined roles of thermal softening and dynamic recrystallization in adiabatic shear banding initiation, *Mech. Mater.* (2018) 117.
- [15] S. Osovski, D. Rittel, P. Landau, et al., Microstructural effects on adiabatic shear band formation, *Scr. Mater.* 66 (2012) 9–12.
- [16] P. Landau, S. Osovski, A. Venkert, et al., The genesis of adiabatic shear bands, *Sci. Rep.* 6 (2016) 37226.
- [17] S. Osovski, D. Rittel, A. Venkert, The respective influence of microstructural and thermal softening on adiabatic shear localization, *Mech. Mater.* 56 (2013) 11–22.
- [18] J.L. Sun, P.W. Trimby, F.K. Yan, et al., Shear banding in commercial pure titanium deformed by dynamic compression, *Acta Mater.* 79 (30) (2014) 47–58.
- [19] C. Ran, P. Chen, L. Li, et al., Dynamic shear deformation and failure of Ti-5Al-5Mo-5V-1Cr-1Fe titanium alloy, *Mater. Sci. Eng. A* 694 (2017) 41–47.
- [20] Z.P. Wan, Y.E. Zhu, H.W. Liu, et al., Microstructure evolution of adiabatic shear bands and mechanisms of saw-tooth chip formation in machining Ti6Al4V, *Mater. Sci. Eng. A* 531 (531) (2012) 155–163.
- [21] C. Tan, H. Tan, X. Liu, et al., Influence of microstructure and strain rate on adiabatic shearing behavior in Ti-6Al-4V alloys, *Mater. Sci. Eng. A* 501 (1) (2009) 30–36.
- [22] Y. Yang, X.M. Li, X.L. Tong, et al., Effects of microstructure on the adiabatic shearing behaviors of titanium alloy, *Mater. Sci. Eng. A* 528 (7–8) (2011) 3130–3133.
- [23] X. Liu, C. Tan, C. Zhang, et al., Correlation of adiabatic shearing behavior with fracture in Ti-6Al-4V alloys with different microstructures, *Int. J. Impact Eng.* 36 (9) (2009) 1143–1149.
- [24] M.A. Meyers, V.F. Nesterenko, J.C. Lasalvia, et al., Shear localization in dynamic deformation of materials: microstructural evolution and self-organization, *Mater. Sci. Eng. A* 317 (1–2) (2001) 204–225.
- [25] Y. Yang, F. Jiang, B.M. Zhou, et al., Microstructural characterization and evolution mechanism of adiabatic shear band in a near beta-Ti alloy, *Mater. Sci. Eng. A* 528 (6) (2011) 2787–2794.
- [26] L. Kuang, Z. Chen, Y. Jiang, et al., Adiabatic shear behaviors in rolled and annealed pure titanium subjected to dynamic impact loading, *Mater. Sci. Eng. A* 685 (2017)

- 95–106.
- [27] H. Zhan, W. Zeng, G. Wang, et al., Microstructural characteristics of adiabatic shear localization in a metastable beta titanium alloy deformed at high strain rate and elevated temperatures, *Mater. Charact.* 102 (2015) 103–113.
- [28] Z. Li, B. Wang, S. Zhao, et al., Dynamic deformation and failure of ultrafine-grained titanium, *Acta Mater.* 125 (2017) 210–218.
- [29] Z. Zeng, S. Jonsson, H.J. Jonsson, The effects of deformation conditions on microstructure and texture of commercially pure Ti, *Acta Mater.* 57 (19) (2009) 5822–5833.
- [30] B. Wang, X. Wang, Z. Li, et al., Shear localization and microstructure in Coarse grained beta titanium alloy, *Mater. Sci. Eng. A* 652 (2016) 287–295.
- [31] Y. Jiang, Z. Chen, C. Zhan, et al., Adiabatic shear localization in pure titanium deformed by dynamic loading: microstructure and microtexture characteristic, *Mater. Sci. Eng. A* 640 (2015) 436–442.
- [32] Y. Yang, F. Jiang, M. Yang, et al., Electron backscatter diffraction analysis of strain distribution in adiabatic shear band and its nearby area in Ti–3Al–5Mo–4.5V alloy, *Mater. Sci. Technol.* 28 (2) (2013) 165–170.
- [33] W.H. Yin, F. Xu, O. Ertorer, et al., Mechanical behavior of microstructure engineered multi-length-scale titanium over a wide range of strain rates, *Acta Mater.* 61 (10) (2013) 3781–3798.
- [34] F.J. Humphreys, Y. Huang, I. Brough, et al., Electron backscatter diffraction of grain and subgrain structures — resolution considerations, *J. Microsc.* 195 (3) (1999) 212–216.
- [35] X. Liu, N.T. Nuhfer, A.D. Nuhfer, et al., Interfacial orientation and misorientation relationships in nanolamellar Cu/Nb composites using transmission-electron-microscope-based orientation and phase mapping, *Acta Mater.* 64 (1) (2014) 333–344.
- [36] H.M. Mourad, C.A. Bronkhorst, V. Livescu, et al., Modeling and simulation framework for dynamic strain localization in elasto-viscoplastic metallic materials subject to large deformations, *Int. J. Plast.* 88 (2017) 1–26.
- [37] I. Ghamarian, Y. Liu, P. Samimi, et al., Development and application of a novel precession electron diffraction technique to quantify and map deformation structures in highly deformed materials—as applied to ultrafine-grained titanium, *Acta Mater.* 79 (79) (2014) 203–215.
- [38] S. Balachandran, S. Kumar, D. Banerjee, On recrystallization of the α and β phases in titanium alloys, *Acta Mater.* (2017).
- [39] H. Mohseni, P. Nandwana, A. Tsoi, et al., In situ nitrided titanium alloys: microstructural evolution during solidification and wear, *Acta Mater.* 83 (83) (2015) 61–74.
- [40] C. Zheng, F. Wang, X. Cheng, et al., Capturing of the propagating processes of adiabatic shear band in Ti–6Al–4V alloys under dynamic compression, *Mater. Sci. Eng. A* 658 (2016) 60–67.
- [41] R.M. Langford, M. Rogers, In situ lift-out: steps to improve yield and a comparison with other FIB TEM sample preparation techniques, *Micron* 39 (8) (2008) 1325–1330.
- [42] M. Schaffer, B. Schaffer, Q. Ramasse, et al., Sample preparation for atomic-resolution STEM at low voltages by FIB, *Ultramicroscopy* 114 (2012) 62–71.
- [43] J.F. Nye, Some geometrical relations in dislocated crystals, *Acta Metall.* 1 (2) (1953) 153–162.
- [44] A. Arsenlis, D.M. Parks, Crystallographic aspects of geometrically-necessary and statistically-stored dislocation density, *Acta Mater.* 47 (5) (1999) 1597–1611.
- [45] W. Pantleon, Resolving the geometrically necessary dislocation content by conventional electron backscattering diffraction, *Scr. Mater.* 58 (11) (2008) 994–997.
- [46] E. Demir, D. Raabe, N. Zaafarani, et al., Investigation of the indentation size effect through the measurement of the geometrically necessary dislocations beneath small indents of different depths using EBSD tomography, *Acta Mater.* 57 (2) (2009) 559–569.
- [47] S. Sun, B.L. Adams, W.E. King, Observations of lattice curvature near the interface of a deformed aluminium bicrystal, *Philos. Mag.* A 80 (1) (2000) 9–25.
- [48] D. He, J. Zhu, Z. Lai, et al., Residual elastic stress–strain field and geometrically necessary dislocation density distribution around nano-indentation in TA15 titanium alloy, *Trans. Nonferrous Met. Soc. China* 23 (1) (2013) 7–13.
- [49] I.G. Dastidar, V. Khademi, T.R. Bieler, et al., The tensile and tensile-creep deformation behavior of Ti–8Al–1Mo–1V(wt%), *Mater. Sci. Eng. A* 636 (2015) 289–300.
- [50] J.A. Rodríguez-Martínez, G. Vadillo, D. Rittel, et al., Dynamic recrystallization and adiabatic shear localization, *Mech. Mater.* 81 (2015) 41–55.